Computational Materials Science 202 (2022) 110942

Contents lists available at ScienceDirect

Computational Materials Science

journal homepage: www.elsevier.com/locate/commatsci

On calculations of basic structural parameters in multi-principal element alloys using small atomistic models

Shuozhi Xu [a], Saeed Zare Chavoshi [b], Yanqing Su [c,*]

[a] Department of Mechanical Engineering, University of California, Santa Barbara, CA 93106-5070, USA
[b] Department of Materials, University of Oxford, Parks Road, Oxford OX1 3PH, UK
[c] Department of Mechanical and Aerospace Engineering, Utah State University, Logan, UT 84322-4130, USA

ARTICLE INFO

Keywords:
Basic structural parameters
Multi-principal element alloys
Atomistic simulations
Embedded-atom method potential
Rules of mixtures

ABSTRACT

Multi-principal element alloys (MPEAs) are alloys that form solid solution phases and consist of three or more principal elements. Fundamental to the numerical study of mechanical properties of MPEAs are the calculations of their basic structural parameters such as lattice parameter and elastic constants. Due to the presence of multiple elements, calculation of each quantity should ideally consider multiple atomic configurations for each MPEA. However, direct calculations are sometimes expensive, and so some studies in the literature either considered only one atomic configuration or used an indirect method to provide an estimation. In this paper, we calculate the lattice parameters, cohesive energies, and elastic constants of 42 equal-molar refractory MPEAs using small atomistic models. For each quantity in each MPEA, four approaches are used: multiple direct calculations using the alloy potential, a single direct calculation using the A-atom potential, as well as estimations using two rules of mixtures. It is shown that the coefficient of variation based on the first approach positively scales with the lattice distortion of MPEAs. In addition, taking the mean values obtained via the first approach as references, we find that the other three approaches can overestimate or underestimate the basic structural parameters.

1. Introduction

Developing high-performance metallic alloys primarily relies on altering chemical compositions and microstructures by introducing foreign elements and/or crystallographic defects [1]. Conventional alloy design focuses on taking one principal metallic element as the matrix and adding small amounts of other elements to enhance particular properties [2]. This strategy results in dilute alloys. In 2004, it was found that some equal-molar compositions of multiple elements can form stable solid solution phases on a simple underlying lattice [3,4]. A new era of alloy design then emerged, producing thousands of novel alloys called multi-principal element alloys (MPEAs) that are at or close to the center of the multi-component phase diagram [5]. In 2010, it was discovered that when the majority of the elements are refractory metals, the MPEAs, termed refractory MPEAs (RMPEAs), can retain excellent mechanical properties at high temperatures [6]. Most RMPEAs are body-centered cubic (BCC) crystals. Take MoNbTi [7] and NbTiZr [8], which possess low densities and high specific strengths, as an example. At room temperature, the two RMPEAs, respectively, have a compressive yield strength of 1100 MPa and 975 MPa [9]. At approximately one half the homologous temperature $0.5T_m$, the compressive yield strengths of MoNbTi and NbTiZr reduce by 53.6% and 48.3% to 510 MPa and 504 MPa, respectively. In contrast, the ultimate tensile strengths of pure refractory metals, e.g., Mo and Nb, drop from 575 MPa and 290 MPa at room temperature to 95 MPa and 77 MPa at $0.5T_m$, respectively [10]. The relative decreases are 83.5% and 73.4%, respectively.

Compared with pure metals and dilute alloys, MPEAs are much more complicated in terms of chemistry. For example, the maximum number of equal-molar MPEAs formed by n chemical elements is

$$N_{\mathrm{MPEA}} = 2^n - \frac{n(n-1)}{2} - n - 1, \tag{1}$$

and N_{MPEA} would become infinite for non-equal-molar MPEAs. As a result, there exist multiple atomic configurations for one MPEA, leading to multiple values for the same quantity, e.g., lattice parameter [11], elastic constants [11], phonon dispersion [12], generalized stacking fault energy [13], vacancy/interstitial formation energies [14], dislocation core energy [15], dislocation core structure [16], stacking fault width [17], local slip resistance [18], as well as critical resolved shear stresses for dislocation gliding [19] and bow-out [20]. Effects of solute concentration [21] and interstitial atoms [22] on basic structural

* Corresponding author.
E-mail address: yanqing.su@usu.edu (Y. Su).

https://doi.org/10.1016/j.commatsci.2021.110942
Received 5 June 2021; Received in revised form 27 September 2021; Accepted 28 September 2021

parameters in MPEAs have also been studied, yet those are beyond the scope of this paper.

The complex chemistry in MPEAs also leads to complex atomic structures, exhibited mainly as lattice distortion and chemical ordering [23]. These chemical and structural characteristics strongly affect the defect dynamics in MPEAs, and hence their mechanical properties [24]. Take dislocation as an example. Compared with pure metals, MPEAs generally have a higher slip resistance [18], a lower dislocation velocity [25], and a larger number of active slip systems [26].

Fundamental to these studies in MPEAs are calculations of basic structural parameters such as lattice parameter and elastic constants [27]. Because of the complex chemistry, calculations should ideally involve multiple simulation cells for one MPEA. A question then arises regarding the cell size. Density functional theory (DFT) calculations in BCC NbTiV and BCC AlNbTiV MPEAs showed that the predicted lattice parameters and elastic constants vary with the computational cell size [28]. A previous atomistic simulation work found that, for the intrinsic stacking fault energy in an equal-molar face-centered cubic (FCC) NiFe alloy, large and small simulation cells, respectively, result in small and large standard deviations while the mean values are almost the same [29]. This suggests that, to obtain an accurate mean value, one either runs a small number of calculations using large cells or a large number of calculations using small cells. In practice, small models are sometimes used, because the calculations, e.g., those based on DFT, are expensive. It is then important to assess the errors associated with using a small number of small models and to explore if the errors could be estimated *a priori*. Sometimes, indirect approaches, e.g., rules of mixtures, are utilized to provide an approximation [13,30–32]. It is necessary to quantify the resultant errors as well.

In this paper, we calculate the basic structural parameters of 42 equal-molar RMPEAs using small atomistic models. For each RMPEA, four approaches are used: multiple direct calculations using the alloy potential, a single direct calculation using the *A*-atom potential, and two rules of mixtures. It is shown that the coefficient of variation based on the first approach positively scales with the lattice distortion of RMPEAs. This finding highlights the importance of considering multiple atomistic structures in calculating basic structural parameters using small models. In addition, taking the mean values obtained via the first approach as references, we find that the other three approaches can overestimate or underestimate the basic structural parameters. While these conclusions are reached based on atomistic simulations [33] in this paper, they are expected to apply to *ab initio* calculations [34] as well.

2. Materials and methods

There are six BCC refractory metals: Cr, Mo, Nb, Ta, V, and W [35]. They can form up to 42 RMPEAs, including 20 ternaries, 15 quaternaries, six quinaries, and one senary. All of them have BCC lattices.

2.1. Alloy potentials

Embedded-atom method (EAM) potentials [36] are used to describe interatomic interactions. The six elemental potentials are: Cr [37], Mo [38], Nb [39], Ta [38], V [40], W [38]. Cross interactions between different elements are based on formulations of Johnson [41] and Zhou et al. [42]. Note that all six elemental potentials have been used in MPEAs, e.g., MoNbTi [13], NbTiZr [16], NbTaV [40], MoNbTaW [43], MoNbTaVW [43], and AlCoCrFeNi [44], wherein the cross interactions were formulated in a similar fashion. In what follows, this type of interatomic potential is called "alloy potential". To assess the accuracy of these potentials, lattice parameters and elastic constants of all pure metals and selected RMPEAs are calculated via DFT in Appendix, and are then compared with those based on MS in Table 1 and Fig. A.1. For the same RMPEA, structural parameters obtained by the alloy potential agree with those by DFT relatively well. We emphasize that the focus of this paper is on comparing different numerical approaches that use the same underlying interatomic potentials. Conclusions based on these comparisons do not necessarily depend on whether the underlying potentials themselves are accurate or not with respect to DFT.

2.2. A-atom potentials

Based on the alloy potential, the "*A*-atom potential" can be constructed to provide a mean-field representation of the RMPEA by approximating the interactions among different elements as a weighted average [45]. Specifically, the *A*-atom EAM formulation for the potential energy is [46]

$$E = \frac{1}{2}\sum_{i}^{N}\sum_{\substack{j\\ j\neq i}}^{N_{\text{nei}}} V_{ij}^{A}(R^{ij}) + \sum_{i}^{N} F_i^{A}\left(\langle\bar{\rho}_i\rangle\right) \tag{2}$$

where N is the number of atoms, N_{nei} is the number of neighboring atoms of atom i, V_{ij} is the pair potential between atoms i and j, F_i is the embedding potential at atom i, $\bar{\rho}^i$ is the host electron density at atom i, R^{ij} is distance between atoms i and j, $\langle\cdots\rangle$ takes the average, and

$$F_i^{A}\left(\langle\bar{\rho}_i\rangle\right) = \sum_{X}^{N_{\text{T}}} c^X F_i^X\left(\langle\bar{\rho}_i\rangle\right) \tag{3}$$

$$V_{ij}^{A}(R^{ij}) = \sum_{X,Y}^{N_{\text{T}}} c^X c^Y V_{ij}^{XY}(R^{ij}) \tag{4}$$

$$\langle\bar{\rho}_i\rangle = \sum_{\substack{j\\ j\neq i}}^{N_{\text{nei}}}\sum_{X}^{N_{\text{T}}} c^X \rho_{ij}^X(R^{ij}) \tag{5}$$

where N_{T} is the number of elemental types, ρ^{ij} is the local electron density contributed by atom j to atom i, and c^X and c^Y are atomic concentrations of elements X and Y, respectively. The *A*-atom potential was shown to provide a good approximation of basic structural parameters in multiple MPEAs, including, but not limited to, FCC CrFeNi [46,47], $Co_{30}Fe_{16.67}Ni_{36.67}Ti_{16.67}$ [48], and CrCoNi [25], as well as BCC $Co_{16.67}Fe_{36.67}Ni_{16.67}Ti_{30}$ [19], NbTiZr [16], and MoNbTi [13].

2.3. Rule of mixtures

In the context of MPEAs, a rule of mixtures is a weighted mean used to predict the value of a quantity p based on that of the constituents. The simple and inverse rules of mixtures, respectively, are

$$p_{\text{up}} = \sum_{i=1}^{n} c_i p_i \tag{6}$$

$$\frac{1}{p_{\text{lo}}} = \sum_{i=1}^{n} \frac{c_i}{p_i} \tag{7}$$

where c_i and p_i are, respectively, the concentration and value of p of element i. When p_i are all positive or all negative, the simple rule of mixtures always yields a higher absolute value than the inverse rule of mixtures. For the lattice parameter, the simple rule of mixtures is usually known as Vegard's law [49]. Note that p_i can come from either *ab initio* or atomistic calculations. In the context of *ab initio* calculations, compared with the results based on alloy structures, in FCC $Ti_{1-x}Al_x$, Tian et al. [50] discovered that the simple rule of mixtures overestimates a_0 and underestimates C_{12} and C_{44} while predicting C_{11} generally well; in three NbTiZr-based RMPEAs, Tian et al. [51] reported that the simple rule of mixtures tends to underestimate a_0 while overestimating elastic constants. Thus, it is interesting to assess whether the inverse rule of mixtures, which has not been applied to MPEAs to our best knowledge, would better predict certain quantities.

2.4. MS simulations

LAMMPS [52] is used for all molecular static (MS) simulations in this paper. For each RMPEA, 20 special quasi-random structures (SQS) [53] are built using ATAT [54]. The tolerance for matching correlations of the SQS and of the ideal random state is set as 0.01. Both pair and triplet correlation functions are considered. The ranges of the pair and triplet correlation, respectively, vary from $2.8a_0$ to $4a_0$ and from $3.6a_0$ to $5.2a_0$, both in increment of $0.4a_0$. Each set of range results in a SQS, and hence 20 SQS in total. The alloy potential is then applied to each SQS. When the A-atom potential or elemental potential is applied, only one atomic structure with all atoms of the same type is considered for each material. Each simulation cell is a cuboid, with ⟨100⟩ crystallographic orientations along all three directions. The numbers of atoms in one cell are 2, 72, 72, 90, and 72 for a pure metal, a ternary, a quaternary, a quinary, and a senary, respectively. These small numbers are chosen because they are commonly used in DFT calculations, to which the conclusion made in this paper is expected to apply.

To calculate the lattice parameter a_0 of each atomic structure, a series of periodic simulation cells of different sizes are used. For each size, the bulk energy is calculated. a_0 is then determined from the cell with the smallest bulk energy. The cohesive energy E_{coh} is the smallest bulk energy divided by the total number of atoms in the cell. This is the so called "energy–volume method", which was shown to yield almost the same results as the "relaxation method" [55]. Based on a_0 of the six pure metals, we can characterize the lattice distortion of each RMPEA [56], i.e.,

$$\delta = \sqrt{\sum_{i=1}^{n} c_i \left(1 - \frac{r_i}{\bar{r}}\right)^2} \tag{8}$$

where $\bar{r} = \sum_{i=1}^{n} c_i r_i$, with r_i being the atomic radius of element i. In BCC crystals, $r_i = (\sqrt{3}/4)a_{0i}$ where a_{0i} is the lattice parameter of element i. Therefore,

$$\delta = \sqrt{\sum_{i=1}^{n} c_i \left(1 - \frac{a_{0i}}{\bar{a}_0}\right)^2} \tag{9}$$

where $\bar{a}_0 = \sum_{i=1}^{n} c_i a_{0i}$.

On the other hand, the stiffness tensor $\boldsymbol{C}$ is calculated via the stress–strain approach [57]. We then calculate the effective BCC elastic constants using the following relationships [13]:

$$C_{11}^{\dagger} = \frac{C_{11} + C_{22} + C_{33}}{3} \tag{10}$$

$$C_{12}^{\dagger} = \frac{C_{12} + C_{13} + C_{23}}{3} \tag{11}$$

$$C_{44}^{\dagger} = \frac{C_{44} + C_{55} + C_{66}}{3} \tag{12}$$

For each of the four basic structural parameters a_0, $C_{11}^{\dagger}$, $C_{12}^{\dagger}$, and $C_{44}^{\dagger}$ in each RMPEA, there are 20 values based on 20 SQS when using the alloy potential. We calculate the mean and standard deviation for each parameter. It follows that the coefficient of variation (CoV) can be obtained by

$$\text{CoV} = \frac{\text{Standard deviation of 20 values}}{\text{Mean of 20 values}} \tag{13}$$

Note that in the cases of A-atom potential and elemental potential, there is only one value for each structural parameter in each RMPEA. Thus, there is no CoV for them.

3. Results and discussions

3.1. Six pure metals

Table 1 presents the lattice parameters a_0, cohesive energies E_{coh}, and three independent elastic constants C_{11}, C_{12}, and C_{44} of the six BCC refractory metals. MS data for Cr, Ta, V, and W are calculated in this work while those for Mo and Nb were recently reported [13]. In Section 3.2, MS data for pure metals will be used to estimate the basic structural parameters in 42 RMPEAs using rules of mixtures (Eqs. (6) and (7)). Data from current and prior DFT calculations [35] and experiments [58,59] are also presented in Table 1 as references. Details of the current DFT calculations are provided in Appendix. Note that the two sets of DFT calculations employed different approaches to calculate the same basic structural parameters in the same metal.

Table 1
Lattice parameter a_0 (in Å), cohesive energy E_{coh} (in eV), elastic constants C_{11}, C_{12}, and C_{44} (in GPa), and Zener ratio A_c, of the six BCC refractory metals. MS data, except those of Mo and Nb [13], are obtained in the current work. In Ref. [35], a_0 and elastic constants were calculated using the volume–energy method and the energy–strain method, respectively. New DFT-based a_0 and elastic constants are calculated using the relaxation method and the stress–strain method, respectively. E_{coh} was calculated in passing when a_0 was calculated. For Cr, DFT and DFT$^{\text{NM}}$ denote calculations wherein antiferromagnetism is and is not considered, respectively. All experimental data are from Ref. [58], except those of E_{coh}, which are from Ref. [59].

Material	Method	a_0	E_{coh}	C_{11}	C_{12}	C_{44}	A_c
Cr	MS	2.881	−4.1	398.03	93.45	103.56	0.68
	DFT$^{\text{NM}}$	2.854	−4.1	483.33	121.23	112.43	0.62
	DFT	2.864	−4.11	427.59	57.67	101.21	0.55
	DFT$^{\text{NM}}$ [35]	2.846	−4.1	494.65	142.37	99.05	0.56
	DFT [35]	2.864	−4.1	429.65	59.94	95	0.51
	Exp [58,59]	2.885	−4.1	348	67	100	0.71
Mo	MS [13]	3.135	−6.81	458.76	167.84	114.32	0.79
	DFT	3.162	−6.35	461.39	160.84	102.87	0.68
	DFT [35]	3.16	−6.35	467.85	158.75	100.22	0.65
	Exp [58,59]	3.147	−6.82	465	163	109	0.72
Nb	MS [13]	3.3	−7.57	263.56	125.28	35.03	0.51
	DFT	3.322	−6.92	242.23	134.92	13.76	0.26
	DFT [35]	3.324	−6.91	249.01	135.43	18.1	0.32
	Exp [58,59]	3.301	−7.57	245	132	28.4	0.5
Ta	MS	3.303	−8.09	262.59	157.74	82.33	1.57
	DFT	3.321	−8.33	258.1	165.11	75.91	1.63
	DFT [35]	3.32	−8.33	268.13	160.35	77.38	1.44
	Exp [58,59]	3.303	−8.1	264	158	82.6	1.56
V	MS	3.026	−5.3	263.93	120.19	38.37	0.53
	DFT	2.999	−5.39	264.61	132.95	24.2	0.37
	DFT [35]	2.999	−5.39	265.97	139.84	26.24	0.42
	Exp [58,59]	3.024	−5.31	230	120	43.1	0.78
W	MS	3.165	−8.76	522.54	204.22	160.76	1.01
	DFT	3.184	−10.17	526.52	199.34	145.39	0.89
	DFT [35]	3.184	−10.41	520.35	199.88	142.42	0.89
	Exp [58,59]	3.165	−8.9	523	203	160	1

It is found that among DFT data, values of the same structural parameter in the same metal obtained by different approaches agree with each other well. This is aligned with a recent work in which different approaches were used to calculate the lattice parameters of four BCC pure metals via either DFT or MS [55]. In addition, and perhaps more importantly, when applying the same approach to the same material, data obtained by DFT and MS agree with each other relatively well, and they both show good agreement with experiments. With regard to a_0, Cr has the smallest value, less than 2.9 Å, while those of all other five elements are larger than 3 Å. According to Eq. (9), the RMPEAs containing Cr are expected to have a large lattice distortion.

Employing the Zener ratio $A_c = 2C_{44}/(C_{11} - C_{12})$ as a measure of the degree of cubic elastic anisotropy, we find that all six pure metals are elastically anisotropic except W. The two most anisotropic metals are Nb, with $A_c = 0.51$, and Ta, with $A_c = 1.57$.

3.2. 42 RMPEAs

The mean lattice parameters $\bar{a}_0$, mean cohesive energies $\bar{E}_{\text{coh}}$, and mean effective elastic constants $\bar{C}_{11}^{\dagger}$, $\bar{C}_{12}^{\dagger}$, and $\bar{C}_{44}^{\dagger}$ of the 42 RMPEAs calculated using the alloy potentials are presented in Tables 2 and 3. These data are used as references against which the data based on A-atom potential and rules of mixture are compared.

Table 2
Mean lattice parameter $\bar{a}_0$ (in Å), mean cohesive energy $\bar{E}_{coh}$ (in eV), mean effective elastic constants $\bar{C}^{\dagger}_{11}$, $\bar{C}^{\dagger}_{12}$, and $\bar{C}^{\dagger}_{44}$ (in GPa), Zener ratio A_c, and lattice distortion δ of 20 ternaries. Results are based on alloy potentials.

Material	$\bar{a}_0$	$\bar{E}_{coh}$	$\bar{C}^{\dagger}_{11}$	$\bar{C}^{\dagger}_{12}$	$\bar{C}^{\dagger}_{44}$	A_c	δ
CrMoNb	3.13	−7.04	247.29	127.38	50.49	0.84	0.055
CrMoTa	3.152	−7.23	262.56	159.11	72.69	1.41	0.056
CrMoV	3.059	−5.79	334.07	114.66	41.91	0.38	0.034
CrMoW	3.113	−7.22	374.59	156.94	81.73	0.75	0.041
CrNbTa	3.194	−7.78	258.76	168.02	68.44	1.51	0.062
CrNbV	3.065	−6.43	234.59	121.65	34.98	0.62	0.056
CrNbW	3.147	−7.79	271.81	172.21	62.29	1.25	0.056
CrTaV	3.1	−6.6	209.21	127.3	36.52	0.89	0.057
CrTaW	3.164	−7.99	301.46	184.88	87.16	1.5	0.056
CrVW	3.073	−6.57	355.59	147.38	52.62	0.51	0.038
MoNbTa	3.243	−7.57	307.17	159.46	77.51	1.05	0.024
MoNbV	3.168	−6.63	276.72	135.23	57.08	0.81	0.036
MoNbW	3.199	−7.75	395.6	172.46	96.16	0.86	0.022
MoTaV	3.18	−6.79	268.4	144.52	72.49	1.17	0.036
MoTaW	3.203	−7.93	388.36	182.9	116.94	1.14	0.023
MoVW	3.146	−6.92	377.6	170.23	88.99	0.86	0.019
NbTaV	3.231	−7.05	215.31	135.15	56.18	1.4	0.04
NbTaW	3.251	−8.15	319.62	162.83	86.09	1.1	0.02
NbVW	3.187	−7.23	296.42	153.65	65.78	0.92	0.035
TaVW	3.196	−7.39	284.1	158.67	82.48	1.32	0.036

Table 3
The same quantities in Table 2, but for 15 quaternaries, six quinaries, and one senary.

Material	$\bar{a}_0$	$\bar{E}_{coh}$	$\bar{C}^{\dagger}_{11}$	$\bar{C}^{\dagger}_{12}$	$\bar{C}^{\dagger}_{44}$	A_c	δ
CrMoNbTa	3.171	−7.13	320.33	144.34	68.68	0.78	0.055
CrMoNbV	3.104	−6.34	307.41	121.43	46.39	0.5	0.05
CrMoNbW	3.138	−7.25	374.5	143.3	77.11	0.67	0.049
CrMoTaV	3.12	−6.46	311.17	138.6	64.04	0.74	0.05
CrMoTaW	3.15	−7.39	381.41	161.67	94.68	0.86	0.049
CrMoVW	3.09	−6.52	402.74	142.92	71.65	0.55	0.036
CrNbTaV	3.15	−6.8	239.86	127.5	53.29	0.95	0.058
CrNbTaW	3.179	−7.85	333.18	161.81	82.03	0.96	0.054
CrNbVW	3.114	−6.9	326.07	143.31	59.7	0.65	0.05
CrTaVW	3.127	−7.04	326.83	155.51	70.69	0.83	0.051
MoNbTaV	3.206	−7	263.72	144.15	66.43	1.11	0.037
MoNbTaW	3.221	−7.84	351.55	172.27	92.18	1.03	0.024
MoNbVW	3.174	−7.13	329.04	156.19	77.11	0.89	0.031
MoTaVW	3.18	−7.25	323.65	165.29	92	1.16	0.031
NbTaVW	3.215	−7.42	273.9	152.28	73.24	1.2	0.036
CrMoNbTaV	3.15	−6.91	287.02	138.33	58.32	0.78	0.052
CrMoNbTaW	3.171	−7.65	343.94	149.92	82.88	0.85	0.049
CrMoNbVW	3.126	−6.93	343.8	137.34	65.29	0.63	0.045
CrMoTaVW	3.135	−7.03	347.46	148.89	78.18	0.79	0.046
CrNbTaVW	3.159	−7.27	286.95	137.76	65.53	0.88	0.052
MoNbTaVW	3.199	−7.33	304.88	157.02	80.77	1.09	0.033
CrMoNbTaVW	3.157	−7.26	316.46	146.46	71.03	0.84	0.047

In terms of the elastic anisotropy, the Zener ratios A_c of 27 RMPEAs are less than 1, while those of the remaining 15 are larger than unity. The majority of RMPEAs have a small to moderate elastic anisotropy. The two most elastically anisotropic RMPEAs are CrMoV, with A_c = 0.38, and CrNbTa, with A_c = 1.51. Note that the lattice distortion only play a minor role in the elastic anisotropy, based on a recent study in FCC binaries and MPEAs [60].

3.2.1. Lattice parameter

As mentioned, when the alloy potential is used, 20 SQS are employed for the lattice parameter calculations in each RMPEA. Fig. 1(a) presents the volume–energy curves obtained in four selected calculations in CrMoNbTa. It is shown that different SQS may lead to different lattice parameters a_0. Averaging 20 a_0 values results in the mean value, $\bar{a}_0$ = 3.171 Å, for CrMoNbTa. The standard deviation in these 20 a_0 is 0.0053 Å. Then following Eq. (13), the CoV of a_0 of CrMoNbTa is 0.0017.

Values of CoV-a_0 of all 42 RMPEAs are plotted with respect to the lattice distortion δ in Fig. 1(b). As expected, RMPEAs containing Cr generally have a larger δ than those without Cr. It is also found that CoV-a_0 scales positively with δ. This finding is similar to the one made by Tian et al. [50]. Using *ab initio* calculations in FCC $Ti_{1-x}Al_x$, they found that the difference in the bulk energy between relaxed and unrelaxed alloy structures scales with the lattice distortion of the binary. All these results suggest that for RMPEAs with a large δ, it is particularly important to involve multiple atomic configurations in calculating $\bar{a}_0$ using the alloy potential.

For CrMoNbTa, *A*-atom potential, simple rule of mixtures, and inverse rule of mixtures predict a_0 = 3.175 Å, 3.155 Å, and 3.145 Å, respectively. All differ from $\bar{a}_0$ predicted by the alloy potential. Values of lattice parameters and cohesive energy in all 42 RMPEAs obtained from four approaches are plotted in Fig. 2. It is found that the four approaches result in a difference in a_0 of less than 0.05 Å and that in E_{coh} of less than 0.5 eV for most RMPEAs. Compared with the alloy potential results, the *A*-atom potential results are the most accurate; however, both rules of mixtures underestimate the lattice parameter while overestimate the cohesive energy in most cases.

3.2.2. Elastic constants

Similar to the case of a_0, the CoV of the effective elastic constants $C^{\dagger}_{ij}$ of each RMPEA using the alloy potential can be obtained by Eq. (13). Values of CoV-$C^{\dagger}_{11}$, CoV-$C^{\dagger}_{12}$, and CoV-$C^{\dagger}_{44}$ of all 42 RMPEAs are plotted with respect to the lattice distortion δ in Fig. 3. Similar to CoV-a_0, each set of CoV-$C^{\dagger}_{ij}$ scales positively with δ of RMPEAs, further highlighting the significance of involving multiple atomic configurations in calculating basic structural parameters using the alloy potential.

Values of the elastic constants in all 42 RMPEAs obtained from four approaches are shown in Fig. 4(a–c). Compared with the alloy potential results, the *A*-atom potential predicts C_{11} reasonably well, but generally underestimates both C_{12} and C_{44}. In the meantime, simple rule of mixtures generally overestimates C_{11}, underestimates C_{12}, and overestimates C_{44}. In addition, inverse rule of mixtures overestimates C_{11}, underestimates C_{12}, yet predicts C_{44} relatively well.

3.2.3. Implications for future research

By using four approaches to calculate the same basic structural parameters in 42 RMPEAs, our results reveal that approximations such as the *A*-atom potential and two rules of mixtures may yield data that much differ from those based on the alloy potential. The relative errors are generally larger for elastic constants than for lattice parameters, in agreement with a previous study in CrFeNi [46]. In the meantime, we note that elastic constants can be used to derive a series of mechanical properties of crystals, e.g., shear modulus, Young's modulus, bulk modulus, Cauchy pressure, Poisson's ratio, Pugh ratio, and Zener ratio [21,22]. Elastic constants are also often among material parameters that enter analytical models for plasticity quantities, e.g., strength, ductility, dislocation core structure, and Peierls stress/barrier. Therefore, inaccurate elastic constants may yield incorrect predictions of material properties. For example, as shown in Fig. 4(d), the *A*-atom potential and inverse rule of mixtures tend to underestimate the Zener ratio A_c, hence predicting more elastically anisotropic RMPEAs. On the other hand, simple rule of mixtures overestimates A_c in about half of the RMPEAs while underestimates A_c in the other half. Another example is that whether a fracture is ductile or brittle is a result of the competition between brittle cleavage and ductile dislocation emission. The former can be quantified by the critical stress intensity for cleavage [61], while the latter by that for dislocation emission [62]. The ratio between the two critical stress intensities, both of which are related to elastic constants, has been employed to analyze the ductility of RMPEAs [63,64].

Our results also shed light on future DFT calculations of structural parameters in MPEAs. In fact, the counterparts of the *A*-atom potential in *ab initio* calculations are the coherent potential approximation (CPA) and the virtual crystal approximation [46]. In the current paper, we find that the *A*-atom potentials predict a_0 and C_{11} well but tend to underestimate C_{12} and C_{44}. On the other hand, compared with the results based on alloy structures, in FCC $Ti_{1-x}Al_x$, Tian et al. [50] showed that, CPA tends to overestimate a_0 and C_{44}, underestimate C_{11}, while predicting C_{12} generally well; then in three NbTiZr-based

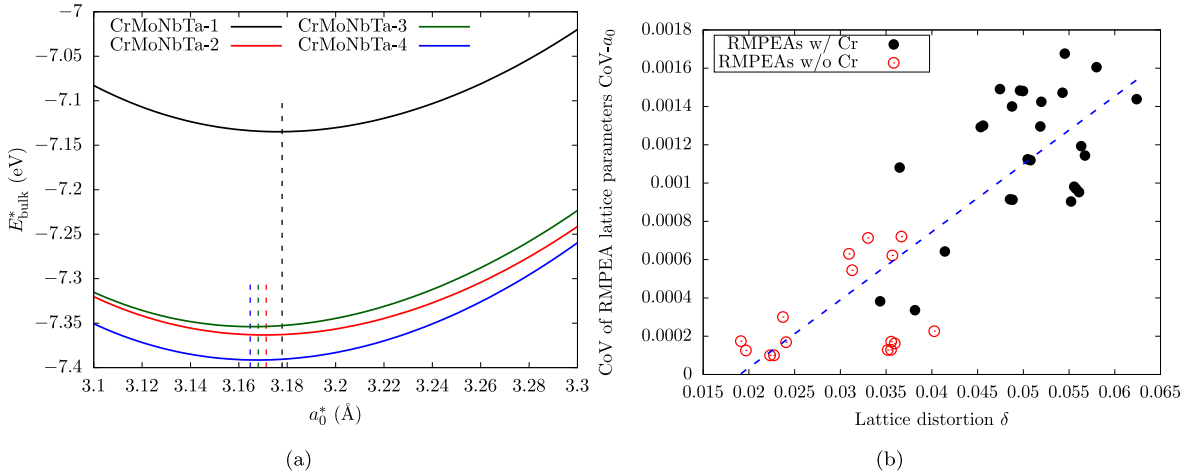

Fig. 1. (a) Bulk energy per atom E^*_{bulk} vs. pre-defined lattice parameter a^*_0 based on four SQS in CrMoNbTa using the alloy potential. Dashed vertical lines indicate the lowest point on each curve. (b) CoV of the lattice parameters of all 42 RMPEAs are plotted with respect to the lattice distortion. The dashed line is the linear fit.

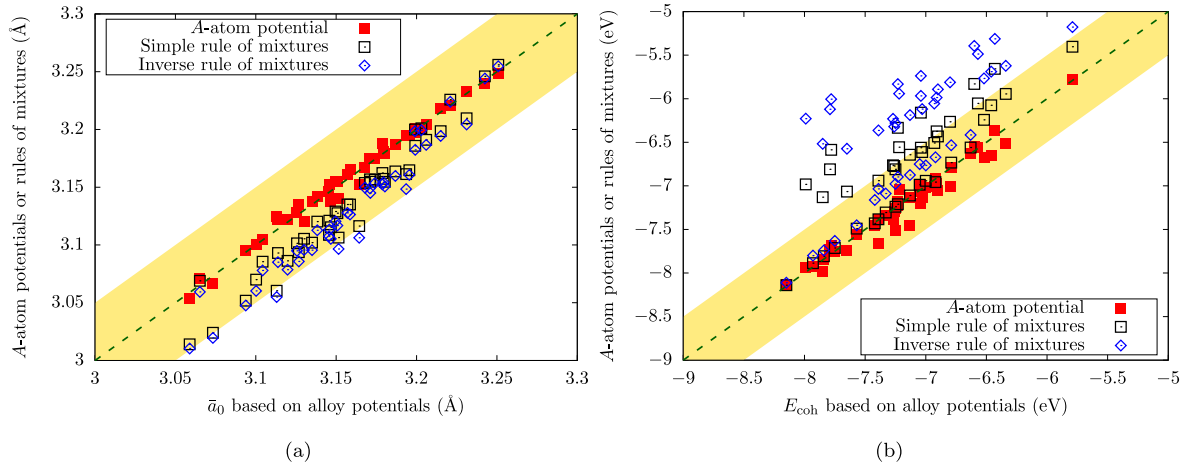

Fig. 2. (a) Lattice parameters and (b) cohesive energies in all 42 RMPEAs obtained from four approaches. The shaded area indicates an agreement with the alloy potential results within (a) 0.05 Å and (b) 0.5 eV.

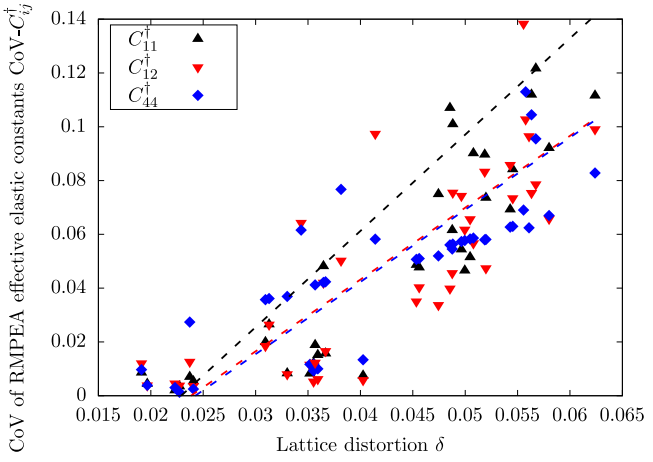

Fig. 3. CoV of the three effective elastic constants of all 42 RMPEAs are plotted with respect to the lattice distortion. Dashed lines are linear fits.

RMPEAs, Tian et al. [51] found that CPA tends to underestimate the lattice parameter a_0 and elastic constant C_{12} while overestimating C_{11} and C_{44}. In dozens of MPEAs, Tian et al. [30], Ge et al. [31], and Huang et al. [32] calculated a_0 and elastic constants using both CPA and simple rule of mixtures. The general finding is that, compared with CPA results, simple rule of mixtures tends to overestimate a_0, and may overestimate or underestimate the elastic constants, depending on the specific constant and MPEA. Taken together, these results imply that caution should be taken when utilizing data based on either *A*-atom potentials in MS simulations, CPA in *ab initio* calculations, or rules of mixtures in either calculation method, especially when the alloy possesses a large lattice distortion. These also suggest that development of new predictive models is necessary.

4. Conclusions

In this work, we conduct MS simulations to calculate the lattice parameters, cohesive energies, and elastic constants of 42 RMPEAs, including 20 ternaries, 15 quaternaries, six quinaries, and one senary. These are all possible RMEPAs formed from the six BCC refractory pure metals: Cr, Mo, Nb, Ta, V, and W. Each quantity in each RMPEA is calculated using four approaches: multiple direct calculations using the alloy potential, a single direct calculation using the *A*-atom potential, and two rules of mixtures.

Based on the first approach, the CoV in both lattice parameters and elastic constants are found to positively scale with the lattice distortion of RMPEAs. This suggests that it is important to consider multiple atomic structures in calculating the basic structural parameters

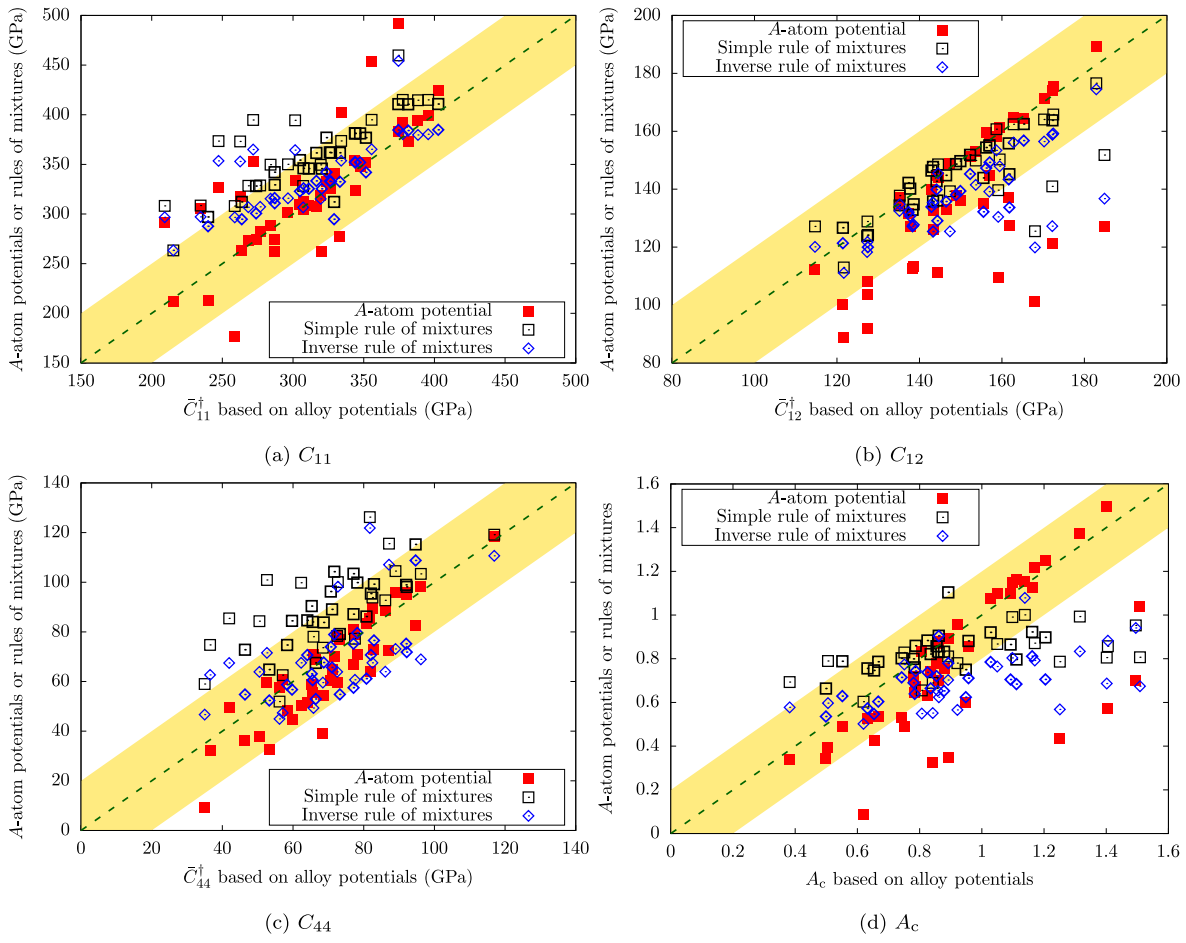

Fig. 4. Three independent elastic constants $C^{\dagger}_{ij}$ and Zener ratio A_c in all 42 RMPEAs obtained from four approaches. The shaded areas indicate an agreement with the alloy potential results within (a) 50 GPa, (b) 20 GPa, (c) 20 GPa, and (d) 0.2, respectively.

using the alloy potential. In general, there exists a discrepancy between the structural parameters obtained by the alloy potential and those predicted by *A*-atom potential and two rules of mixtures. Specifically, for the lattice parameter a_0 and cohesive energy E_{coh}, the *A*-atom potentials provide good predictions while both rules of mixtures tend to underestimate a_0 while overestimate E_{coh}. For the elastic constants, the *A*-atom potential predicts C_{11} reasonably well, but generally underestimates both C_{12} and C_{44}. In the meantime, simple rule of mixtures generally overestimates C_{11}, underestimates C_{12}, and overestimates C_{44}, whilst inverse rule of mixtures overestimates C_{11}, underestimates C_{12}, yet predicts C_{44} relatively well.

CRediT authorship contribution statement

Shuozhi Xu: Conceptualization, Methodology, Formal analysis, Investigation, Data curation, Writing – original draft, Writing – review & editing. **Saeed Zare Chavoshi:** Validation, Formal analysis, Writing – review & editing. **Yanqing Su:** Software, Resources, Writing – review & editing, Funding acquisition.

Declaration of competing interest

The authors declare that they have no known competing financial interests or personal relationships that could have appeared to influence the work reported in this paper.

Data availability

The data that support the findings of this study are available from Dr. Yanqing Su (email: yanqing.su@usu.edu) upon reasonable request.

Acknowledgments

We thank Prof. Francesco Maresca for providing the EAM potential parameters for V, Mr. Wurong Jian for providing all *A*-atom potentials, and Prof. Leonid V. Zhigilei and Dr. Miao He for helpful discussions. This work used the Extreme Science and Engineering Discovery Environment (XSEDE), which is supported by National Science Foundation, USA grant number ACI-1053575. The support and resources from the Center for High Performance Computing at the University of Utah, USA are also gratefully acknowledged.

Appendix. Basic structural parameters calculated via DFT

To validate the alloy potentials, lattice parameters and elastic constants of six pure metals and 26 Cr-based RMPEAs are calculated via DFT using VASP [65]. DFT parameters closely follow prior work of some co-authors of this paper [35,66] for BCC pure metals. Based on the projector augmented wave method [67,68], a plane-wave basis with a cutoff energy of 398.52 eV is adopted. To approximate the exchange–correlation energy functional, the Perdew–Burke–Ernzerhof formulation of the generalized gradient approximation [69] is used. The Brillouin zone is constructed by the Monkhorst–Pack scheme [70], with a smearing width of 0.2 eV based on the Methfessel–Paxton smearing method [71]. The *k*-point meshes are $11 \times 11 \times 11$ in pure metals and $5 \times 5 \times 5$ in RMPEAs. The conjugate gradient scheme is employed for the electronic self-consistent loop; the convergence is reached when the total free energy change between two steps is smaller than 10^{-4} eV [72]. To yield results that are better comparable with MS, spin-polarization is not considered.

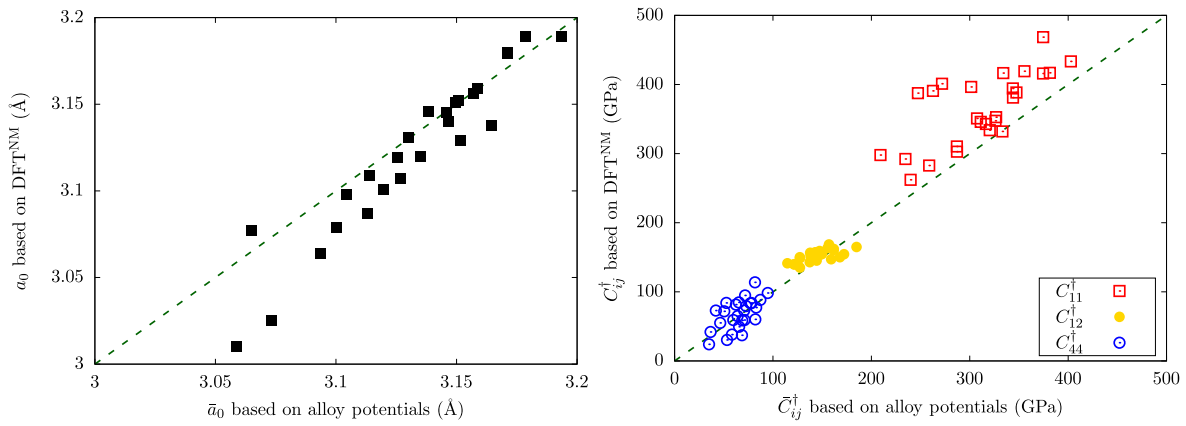

(a) Lattice parameter (b) Elastic constants

Fig. A.1. (a) Lattice parameters and (b) elastic constants in 26 Cr-based RMPEAs obtained from MS simulations using alloy potentials and DFT calculations without spin-polarization, denoted by the superscript NM.

Specifically, lattice parameters are calculated using the relaxation method while elastic constants are based on the stress–strain method. DFT results for pure metals are presented in Table 1 and those for RMPEAs are in Fig. A.1, all against MS results based on alloy potentials. Because DFT calculations are expensive, only one SQS, which has the largest pair and triplet correlation ranges as described in Section 2.4, is considered for each RMPEA.

References

[1] X. Li, K. Lu, Playing with defects in metals, Nature Mater. 16 (2017) 700–701, http://dx.doi.org/10.1038/nmat4929, URL https://www.nature.com/articles/nmat4929.

[2] I.J. Beyerlein, S. Xu, J. Llorca, J.A. El-Awady, J.R. Mianroodi, B. Svendsen, Alloy design for mechanical properties: Conquering the length scales, MRS Bull. 44 (4) (2019) 257–265, http://dx.doi.org/10.1557/mrs.2019.67.

[3] J.-W. Yeh, S.-K. Chen, S.-J. Lin, J.-Y. Gan, T.-S. Chin, T.-T. Shun, C.-H. Tsau, S.-Y. Chang, Nanostructured high-entropy alloys with multiple principal elements: Novel alloy design concepts and outcomes, Adv. Eng. Mater. 6 (5) (2004) 299–303, http://dx.doi.org/10.1002/adem.200300567, URL https://onlinelibrary.wiley.com/doi/abs/10.1002/adem.200300567.

[4] B. Cantor, I.T.H. Chang, P. Knight, A.J.B. Vincent, Microstructural development in equiatomic multicomponent alloys, Mater. Sci. Eng. A 375–377 (2004) 213–218, http://dx.doi.org/10.1016/j.msea.2003.10.257, URL http://www.sciencedirect.com/science/article/pii/S0921509303009936.

[5] Z. Li, S. Zhao, R.O. Ritchie, M.A. Meyers, Mechanical properties of high-entropy alloys with emphasis on face-centered cubic alloys, Prog. Mater. Sci. 102 (2019) 296–345, http://dx.doi.org/10.1016/j.pmatsci.2018.12.003, URL http://www.sciencedirect.com/science/article/pii/S0079642518301178.

[6] O.N. Senkov, G.B. Wilks, D.B. Miracle, C.P. Chuang, P.K. Liaw, Refractory high-entropy alloys, Intermetallics 18 (9) (2010) 1758–1765, http://dx.doi.org/10.1016/j.intermet.2010.05.014, URL http://www.sciencedirect.com/science/article/pii/S0966979510002475.

[7] O.N. Senkov, S.I. Rao, T.M. Butler, K.J. Chaput, Ductile Nb alloys with reduced density and cost, J. Alloys Compd. 808 (2019) 151685, http://dx.doi.org/10.1016/j.jallcom.2019.151685, URL http://www.sciencedirect.com/science/article/pii/S0925838819329184.

[8] O.N. Senkov, S. Rao, K.J. Chaput, C. Woodward, Compositional effect on microstructure and properties of NbTiZr-based complex concentrated alloys, Acta Mater. 151 (2018) 201–215, http://dx.doi.org/10.1016/j.actamat.2018.03.065, URL http://www.sciencedirect.com/science/article/pii/S1359645418302635.

[9] O.N. Senkov, S. Gorsse, D.B. Miracle, High temperature strength of refractory complex concentrated alloys, Acta Mater. 175 (2019) 394–405, http://dx.doi.org/10.1016/j.actamat.2019.06.032, URL http://www.sciencedirect.com/science/article/pii/S1359645419304033.

[10] J.B. Lambert, Refractory metals and alloys, in: ASM Handbook Volume 2: Properties and Selection: Nonferrous Alloys and Special-Purpose Materials, ASM International, 1990, URL https://dl.asminternational.org/handbooks/book/14/chapter/201131/Refractory-Metals-and-Alloys.

[11] Y. Su, S. Xu, I.J. Beyerlein, *Ab initio*-informed phase-field modeling of dislocation core structures in equal-molar CoNiRu multi-principal element alloys, Modelling Simul. Mater. Sci. Eng. 27 (8) (2019) 084001, http://dx.doi.org/10.1088/1361-651X/ab3b62.

[12] Q.-J. Li, H. Sheng, E. Ma, Strengthening in multi-principal element alloys with local-chemical-order roughened dislocation pathways, Nat. Commun. 10 (2019) 3563, http://dx.doi.org/10.1038/s41467-019-11464-7, URL https://www.nature.com/articles/s41467-019-11464-7.

[13] S. Xu, E. Hwang, W.-R. Jian, Y. Su, I.J. Beyerlein, Atomistic calculations of the generalized stacking fault energies in two refractory multi-principal element alloys, Intermetallics 124 (2020) 106844.

[14] R. Gröger, V. Vitek, A. Dlouhý, Effective pair potential for random fcc CoCrFeMnNi alloys, Modelling Simul. Mater. Sci. Eng. 28 (7) (2020) 075006, http://dx.doi.org/10.1088/1361-651X/ab7f8b.

[15] S. Yin, J. Ding, M. Asta, R.O. Ritchie, Ab initio modeling of the energy landscape for screw dislocations in body-centered cubic high-entropy alloys, npj Comput. Mater. 6 (2020) 110, http://dx.doi.org/10.1038/s41524-020-00377-5, URL https://www.nature.com/articles/s41524-020-00377-5.

[16] S.I. Rao, B. Akdim, E. Antillon, C. Woodward, T.A. Parthasarathy, O.N. Senkov, Modeling solution hardening in BCC refractory complex concentrated alloys: NbTiZr, $Nb_{1.5}TiZr_{0.5}$ and $Nb_{0.5}TiZr_{1.5}$, Acta Mater. 168 (2019) 222–236, http://dx.doi.org/10.1016/j.actamat.2019.02.013, URL http://www.sciencedirect.com/science/article/pii/S1359645419300916.

[17] W. Li, S.I. Rao, Q. Wang, H. Fan, J. Yang, J.A. El-Awady, Core structure and mobility of edge dislocations in face-centered-cubic chemically complex NiCoFe and NiCoFeCu equiatomic solid-solution alloys, Materialia 9 (2020) 100628, http://dx.doi.org/10.1016/j.mtla.2020.100628, URL http://www.sciencedirect.com/science/article/pii/S2589152920300454.

[18] S. Xu, Y. Su, W.-R. Jian, I.J. Beyerlein, Local slip resistances in equal-molar MoNbTi multi-principal element alloy, Acta Mater. 202 (2021) 68–79, http://dx.doi.org/10.1016/j.actamat.2020.10.042, URL http://www.sciencedirect.com/science/article/pii/S1359645420308405.

[19] S.I. Rao, C. Varvenne, C. Woodward, T.A. Parthasarathy, D. Miracle, O.N. Senkov, W.A. Curtin, Atomistic simulations of dislocations in a model BCC multicomponent concentrated solid solution alloy, Acta Mater. 125 (2017) 311–320, http://dx.doi.org/10.1016/j.actamat.2016.12.011, URL http://www.sciencedirect.com/science/article/pii/S1359645416309478.

[20] L.T.W. Smith, Y. Su, S. Xu, A. Hunter, I.J. Beyerlein, The effect of local chemical ordering on Frank-Read source activation in a refractory multi-principal element alloy, Int. J. Plast. 134 (2020) 102850, http://dx.doi.org/10.1016/j.ijplas.2020.102850, URL http://www.sciencedirect.com/science/article/pii/S0749641920304885.

[21] Q. Zhao, J. Li, Q. Fang, H. Feng, Effect of Al solute concentration on mechanical properties of Al_xFeCuCrNi high-entropy alloys: A first-principles study, Phys. B: Condens. Matter. 566 (2019) 30–37, http://dx.doi.org/10.1016/j.physb.2019.04.025, URL https://www.sciencedirect.com/science/article/pii/S0921452619302571.

[22] Y. Chen, Q. Zhao, H. Wu, Q. Fang, J. Li, Effect of interstitial N atom on physical and mechanical properties of FeCoCrNiMn high-entropy alloys: A first-principles study, Phys. B: Condens. Matter 615 (2021) 413078, http://dx.doi.org/10.1016/j.physb.2021.413078, URL https://www.sciencedirect.com/science/article/pii/S0921452621002684.

[23] X.-G. Li, C. Chen, H. Zheng, Y. Zuo, S.P. Ong, Complex strengthening mechanisms in the NbMoTaW multi-principal element alloy, npj Comput. Mater. 6 (2020) 70, http://dx.doi.org/10.1038/s41524-020-0339-0, URL https://www.nature.com/articles/s41524-020-0339-0.

[24] W.G. Nöhring, W.A. Curtin, Design using randomness: a new dimension for metallurgy, Scr. Mater. 187 (2020) 210–215, http://dx.doi.org/10.1016/j.scriptamat.2020.06.012, URL http://www.sciencedirect.com/science/article/pii/S1359646220303651.

[25] W.-R. Jian, Z. Xie, S. Xu, Y. Su, X. Yao, I.J. Beyerlein, Effects of lattice distortion and chemical short-range order on the mechanisms of deformation in medium entropy alloy CoCrNi, Acta Mater. 199 (2020) 352–369, http://dx.doi.org/10.1016/j.actamat.2020.08.044, URL http://www.sciencedirect.com/science/article/pii/S1359645420306492.

[26] F. Wang, G.H. Balbus, S. Xu, Y. Su, J. Shin, P.F. Rottmann, K.E. Knipling, J.-C. Stinville, L.H. Mills, O.N. Senkov, I.J. Beyerlein, T.M. Pollock, D.S. Gianola, Multiplicity of dislocation pathways in a refractory multiprincipal element alloy, Science 370 (6512) (2020) 95–101, http://dx.doi.org/10.1126/science.aba3722, URL https://science.sciencemag.org/content/370/6512/95.

[27] S. Huang, F. Tian, L. Vitos, Elasticity of high-entropy alloys from ab initio theory, J. Mater. Res. 33 (19) (2018) 2938–2953, http://dx.doi.org/10.1557/jmr.2018.237, URL https://www.cambridge.org/core/journals/journal-of-materials-research/article/elasticity-of-highentropy-alloys-from-ab-initio-theory/D3630662FC5274E575411A3FB517DC0E.

[28] F. Tian, Y. Wang, L. Vitos, Impact of aluminum doping on the thermophysical properties of refractory medium-entropy alloys, J. Appl. Phys. 121 (1) (2017) 015105, http://dx.doi.org/10.1063/1.4973489, URL https://aip.scitation.org/doi/10.1063/1.4973489.

[29] S. Zhao, Y. Osetsky, G.M. Stocks, Y. Zhang, Local-environment dependence of stacking fault energies in concentrated solid-solution alloys, npj Comput. Mater. 5 (1) (2019) 13, http://dx.doi.org/10.1038/s41524-019-0150-y, URL https://www.nature.com/articles/s41524-019-0150-y.

[30] F. Tian, L.K. Varga, N. Chen, J. Shen, L. Vitos, *Ab initio* design of elastically isotropic $TiZrNbMoV_x$ high-entropy alloys, J. Alloys Compd. 599 (2014) 19–25, http://dx.doi.org/10.1016/j.jallcom.2014.01.237, URL http://www.sciencedirect.com/science/article/pii/S0925838814003089.

[31] H. Ge, F. Tian, Y. Wang, Elastic and thermal properties of refractory high-entropy alloys from first-principles calculations, Comput. Mater. Sci. 128 (2017) 185–190, http://dx.doi.org/10.1016/j.commatsci.2016.11.035, URL http://www.sciencedirect.com/science/article/pii/S0927025616305961.

[32] S. Huang, E. Holmström, O. Eriksson, L. Vitos, Mapping the magnetic transition temperatures for medium- and high-entropy alloys, Intermetallics 95 (2018) 80–84, http://dx.doi.org/10.1016/j.intermet.2018.01.016, URL http://www.sciencedirect.com/science/article/pii/S0966979517311688.

[33] A. Ferrari, B. Dutta, K. Gubaev, Y. Ikeda, P. Srinivasan, B. Grabowski, F. Körmann, Frontiers in atomistic simulations of high entropy alloys, J. Appl. Phys. 128 (15) (2020) 150901, http://dx.doi.org/10.1063/5.0025310, URL https://aip.scitation.org/doi/full/10.1063/5.0025310.

[34] Y. Ikeda, B. Grabowski, F. Körmann, *Ab initio* phase stabilities and mechanical properties of multicomponent alloys: A comprehensive review for high entropy alloys and compositionally complex alloys, Mater. Charact. 147 (2019) 464–511, http://dx.doi.org/10.1016/j.matchar.2018.06.019, URL https://www.sciencedirect.com/science/article/pii/S1044580318306636.

[35] S. Xu, Y. Su, L.T.W. Smith, I.J. Beyerlein, Frank-Read source operation in six body-centered cubic refractory metals, J. Mech. Phys. Solids 141 (2020) 104017, http://dx.doi.org/10.1016/j.jmps.2020.104017, URL http://www.sciencedirect.com/science/article/pii/S0022509620302520.

[36] M.S. Daw, M.I. Baskes, Embedded-atom method: Derivation and application to impurities, surfaces, and other defects in metals, Phys. Rev. B 29 (12) (1984) 6443–6453, http://dx.doi.org/10.1103/PhysRevB.29.6443.

[37] Z. Lin, R.A. Johnson, L.V. Zhigilei, Computational study of the generation of crystal defects in a bcc metal target irradiated by short laser pulses, Phys. Rev. B 77 (21) (2008) 214108, http://dx.doi.org/10.1103/PhysRevB.77.214108, URL https://link.aps.org/doi/10.1103/PhysRevB.77.214108.

[38] X.W. Zhou, R.A. Johnson, H.N.G. Wadley, Misfit-energy-increasing dislocations in vapor-deposited cofe/nife multilayers, Phys. Rev. B 69 (14) (2004) 144113, http://dx.doi.org/10.1103/PhysRevB.69.144113, URL http://link.aps.org/doi/10.1103/PhysRevB.69.144113.

[39] D.-Y. Lin, S.S. Wang, D.L. Peng, M. Li, X.D. Hui, An *n*-body potential for a Zr-Nb system based on the embedded-atom method, J. Phys.: Condens. Matter 25 (10) (2013) 105404, http://dx.doi.org/10.1088/0953-8984/25/10/105404.

[40] A. Ghafarollahi, F. Maresca, W.A. Curtin, Solute/screw dislocation interaction energy parameter for strengthening in bcc dilute to high entropy alloys, Modelling Simul. Mater. Sci. Eng. 27 (8) (2019) 085011, http://dx.doi.org/10.1088/1361-651X/ab4969.

[41] R.A. Johnson, Alloy models with the embedded-atom method, Phys. Rev. B 39 (17) (1989) 12554–12559, http://dx.doi.org/10.1103/PhysRevB.39.12554, URL https://link.aps.org/doi/10.1103/PhysRevB.39.12554.

[42] X.W. Zhou, H.N.G. Wadley, R.A. Johnson, D.J. Larson, N. Tabat, A. Cerezo, A.K. Petford-Long, G.D.W. Smith, P.H. Clifton, R.L. Martens, T.F. Kelly, Atomic scale structure of sputtered metal multilayers, Acta Mater. 49 (19) (2001) 4005–4015, http://dx.doi.org/10.1016/S1359-6454(01)00287-7, URL http://www.sciencedirect.com/science/article/pii/S1359645401002877.

[43] F. Maresca, W.A. Curtin, Mechanistic origin of high strength in refractory BCC high entropy alloys up to 1900K, Acta Mater. 182 (2020) 235–249, http://dx.doi.org/10.1016/j.actamat.2019.10.015, URL http://www.sciencedirect.com/science/article/pii/S1359645419306755.

[44] A. Fourmont, S. Le Gallet, O. Politano, C. Desgranges, F. Baras, Effects of planetary ball milling on AlCoCrFeNi high entropy alloys prepared by Spark Plasma Sintering: Experiments and molecular dynamics study, J. Alloys Compd. 820 (2020) 153448, http://dx.doi.org/10.1016/j.jallcom.2019.153448, URL http://www.sciencedirect.com/science/article/pii/S0925838819346948.

[45] R.W. Smith, G.S. Was, Application of molecular dynamics to the study of hydrogen embrittlement in Ni-Cr-Fe alloys, Phys. Rev. B 40 (15) (1989) 10322–10336, http://dx.doi.org/10.1103/PhysRevB.40.10322, URL https://link.aps.org/doi/10.1103/PhysRevB.40.10322.

[46] C. Varvenne, A. Luque, W.G. Nöhring, W.A. Curtin, Average-atom interatomic potential for random alloys, Phys. Rev. B 93 (10) (2016) 104201, http://dx.doi.org/10.1103/PhysRevB.93.104201, URL https://link.aps.org/doi/10.1103/PhysRevB.93.104201.

[47] W.G. Nöhring, W.A. Curtin, Thermodynamic properties of average-atom interatomic potentials for alloys, Modelling Simul. Mater. Sci. Eng. 24 (4) (2016) 045017, http://dx.doi.org/10.1088/0965-0393/24/4/045017.

[48] S.I. Rao, C. Woodward, T.A. Parthasarathy, O. Senkov, Atomistic simulations of dislocation behavior in a model FCC multicomponent concentrated solid solution alloy, Acta Mater. 134 (2017) 188–194, http://dx.doi.org/10.1016/j.actamat.2017.05.071, URL http://www.sciencedirect.com/science/article/pii/S1359645417304603.

[49] A.R. Denton, N.W. Ashcroft, Vegard's law, Phys. Rev. A 43 (6) (1991) 3161–3164, http://dx.doi.org/10.1103/PhysRevA.43.3161, URL https://link.aps.org/doi/10.1103/PhysRevA.43.3161.

[50] L.-Y. Tian, Q.-M. Hu, R. Yang, J. Zhao, B. Johansson, L. Vitos, Elastic constants of random solid solutions by SQS and CPA approaches: the case of fcc Ti-Al, J. Phys.: Condens. Matter 27 (31) (2015) 315702, http://dx.doi.org/10.1088/0953-8984/27/31/315702.

[51] L.-Y. Tian, G. Wang, J.S. Harris, D.L. Irving, J. Zhao, L. Vitos, Alloying effect on the elastic properties of refractory high-entropy alloys, Mater. Des. 114 (2017) 243–252, http://dx.doi.org/10.1016/j.matdes.2016.11.079, URL http://www.sciencedirect.com/science/article/pii/S0264127516314794.

[52] S. Plimpton, Fast parallel algorithms for short-range molecular dynamics, J. Comput. Phys. 117 (1) (1995) 1–19, http://dx.doi.org/10.1006/jcph.1995.1039, URL http://www.sciencedirect.com/science/article/pii/S002199918571039X.

[53] A. Zunger, S.-H. Wei, L.G. Ferreira, J.E. Bernard, Special quasirandom structures, Phys. Rev. Lett. 65 (3) (1990) 353–356, http://dx.doi.org/10.1103/PhysRevLett.65.353, URL https://link.aps.org/doi/10.1103/PhysRevLett.65.353.

[54] A. van de Walle, P. Tiwary, M. de Jong, D. Olmsted, M. Asta, A. Dick, D. Shin, Y. Wang, L.-Q. Chen, Z.K. Liu, Efficient stochastic generation of special quasirandom structures, CALPHAD 42 (2013) 13–18, http://dx.doi.org/10.1016/j.calphad.2013.06.006, URL http://www.sciencedirect.com/science/article/pii/S0364591613000540.

[55] X. Wang, S. Xu, W.-R. Jian, X.-G. Li, Y. Su, I.J. Beyerlein, Generalized stacking fault energies and peierls stresses in refractory body-centered cubic metals from machine learning-based interatomic potentials, Comput. Mater. Sci. 192 (2021) 110364.

[56] Y. Zhang, Y.J. Zhou, J.P. Lin, G.L. Chen, P.K. Liaw, Solid-solution phase formation rules for multi-component alloys, Adv. Eng. Mater. 10 (6) (2008) 534–538, http://dx.doi.org/10.1002/adem.200700240.

[57] W.-R. Jian, S. Xu, I.J. Beyerlein, On the significance of model design in atomistic calculations of the Peierls stress in Nb, Comput. Mater. Sci. 188 (2021) 110150.

[58] H. Warlimont, W. Martienssen (Eds.), Springer handbook of materials data, second ed., in: Springer Handbooks, Springer International Publishing, 2018, URL https://www.springer.com/us/book/9783319697413.

[59] C. Kittel, Introduction To Solid State Physics, eighth ed., Wiley, Hoboken, NJ, 2004.

[60] C.-C. Yen, G.-R. Huang, Y.-C. Tan, H.-W. Yeh, D.-J. Luo, K.-T. Hsieh, E.-W. Huang, J.-W. Yeh, S.-J. Lin, C.-C. Wang, C.-L. Kuo, S.-Y. Chang, Y.-C. Lo, Lattice distortion effect on elastic anisotropy of high entropy alloys, J. Alloys Compd. 818 (2020) 152876, http://dx.doi.org/10.1016/j.jallcom.2019.152876, URL https://www.sciencedirect.com/science/article/pii/S0925838819341222.

[61] A.A. Griffith, VI. the phenomena of rupture and flow in solids, Phil. Trans. R. Soc. A 221 (582–593) (1921) 163–198, http://dx.doi.org/10.1098/rsta.1921.0006, URL https://royalsocietypublishing.org/doi/10.1098/rsta.1921.0006.

[62] J.R. Rice, Dislocation nucleation from a crack tip: An analysis based on the Peierls concept, J. Mech. Phys. Solids 40 (2) (1992) 239–271, http://dx.doi.org/10.1016/S0022-5096(05)80012-2, URL http://www.sciencedirect.com/science/article/pii/S0022509605800122.

[63] X. Li, W. Li, D.L. Irving, L.K. Varga, L. Vitos, S. Schönecker, Ductile and brittle crack-tip response in equimolar refractory high-entropy alloys, Acta Mater. 189 (2020) 174–187, http://dx.doi.org/10.1016/j.actamat.2020.03.004, URL https://www.sciencedirect.com/science/article/pii/S1359645420301816.

[64] E. Mak, B. Yin, W.A. Curtin, A ductility criterion for bcc high entropy alloys, J. Mech. Phys. Solids 152 (2021) 104389, http://dx.doi.org/10.1016/j.jmps.2021.104389, URL https://www.sciencedirect.com/science/article/pii/S0022509621000776.

[65] G. Kresse, J. Furthmüller, Efficient iterative schemes for *ab initio* total-energy calculations using a plane-wave basis set, Phys. Rev. B 54 (16) (1996) 11169–11186, http://dx.doi.org/10.1103/PhysRevB.54.11169, URL http://link.aps.org/doi/10.1103/PhysRevB.54.11169.

[66] Y. Su, M. Ardeljan, M. Knezevic, M. Jain, S. Pathak, I.J. Beyerlein, Elastic constants of pure body-centered cubic Mg in nanolaminates, Comput. Mater. Sci. 174 (2020) 109501, http://dx.doi.org/10.1016/j.commatsci.2019.109501, URL http://www.sciencedirect.com/science/article/pii/S0927025619308006.

[67] P.E. Blöchl, Projector augmented-wave method, Phys. Rev. B 50 (24) (1994) 17953–17979, http://dx.doi.org/10.1103/PhysRevB.50.17953, URL http://link.aps.org/doi/10.1103/PhysRevB.50.17953.

[68] G. Kresse, D. Joubert, From ultrasoft pseudopotentials to the projector augmented-wave method, Phys. Rev. B 59 (3) (1999) 1758–1775, http://dx.doi.org/10.1103/PhysRevB.59.1758, URL http://link.aps.org/doi/10.1103/PhysRevB.59.1758.

[69] J.P. Perdew, K. Burke, M. Ernzerhof, Generalized gradient approximation made simple, Phys. Rev. Lett. 77 (18) (1996) 3865–3868, http://dx.doi.org/10.1103/PhysRevLett.77.3865, URL http://link.aps.org/doi/10.1103/PhysRevLett.77.3865.

[70] H.J. Monkhorst, J.D. Pack, Special points for Brillouin-zone integrations, Phys. Rev. B 13 (12) (1976) 5188–5192, http://dx.doi.org/10.1103/PhysRevB.13.5188, URL https://link.aps.org/doi/10.1103/PhysRevB.13.5188.

[71] M. Methfessel, A.T. Paxton, High-precision sampling for Brillouin-zone integration in metals, Phys. Rev. B 40 (6) (1989) 3616–3621, http://dx.doi.org/10.1103/PhysRevB.40.3616, URL http://link.aps.org/doi/10.1103/PhysRevB.40.3616.

[72] Y. Su, S. Xu, I.J. Beyerlein, Density functional theory calculations of generalized stacking fault energy surfaces for eight face-centered cubic transition metals, J. Appl. Phys. 126 (10) (2019) 105112, http://dx.doi.org/10.1063/1.5115282, URL https://aip.scitation.org/doi/10.1063/1.5115282.